mater.scichina.com link.springer.com Published online 12 April 2024 | https://doi.org/10.1007/s40843-023-2802-8

Semimetallic hydroxide materials for electrochemical water oxidation

Jing Wang[1], Mohammed-Ibrahim Jamesh[2], Qiang Gao[1], Bo Han[1], Ruimin Sun[1], Hsien-Yi Hsu[2], Chenggang Zhou[1] and Zhao Cai[1*]

ABSTRACT Searching for catalyst materials with high intrinsic activity for water oxidation holds the key to numerous clean energy technologies. Hydroxide semiconductors are electrochemically active to drive oxygen evolution reaction (OER), but suffer from poor electronic conductivity, restricting their intrinsic electrocatalytic activity. Here, a semimetallic hydroxide material was designed as efficient OER catalyst with both improved electronic conductivity and intrinsic electrocatalytic activity. By cationic doping and anionic vacancy manipulation, the NiFe layered double hydroxide (LDH) semiconductor was turned into semi-metallic with two orders of magnitude lower resistivity. Consequently, the semimetallic LDH (SM LDH) array electrode exhibited an intrinsically improved OER activity with a low overpotential of 195 mV at 10 mA cm^{-2} and a low Tafel slope of 40.9 mV dec^{-1} in alkaline medium, outperforming commercial RuO_2 catalysts (316 mV, 99.6 mV dec^{-1}) under the same test condition. In-depth Raman and first-principles calculations demonstrated that the enhanced OER intrinsic activity of SM LDH was associated with the high electronic conductivity, which promoted the formation and stabilization of high-valence metal sites in oxyhydroxide intermediates. These finding suggest semi-metallic hydroxides as an advanced electrode material with both fascinating electric and catalytic properties.

Keywords: electrocatalyst, hydroxide, semi-metal, electric conductivity, intrinsic activity

INTRODUCTION

Water oxidation is a key half-cell reaction that limits the efficiency of various clean energy technologies (e.g., water splitting and metal-air batteries) towards the way to a carbon neutral society in future [1–11]. However, the oxygen evolution reaction (OER) kinetics is generally sluggish due to the electrochemical nature of such multiple proton-coupled electron transfer processes [12–15]. Exploring efficient catalyst materials is of paramount importance to improve the OER rate and the energy efficiency of those energy technologies [16–22]. To date, noble metal-based oxide materials, typically IrO_2 and RuO_2, are the state-of-the-art OER catalysts, but their wide practical use has been restricted by the high cost [23,24]. Therefore, developing low-cost catalyst materials with high intrinsic OER activity is imperative for promoting energy technological advance.

NiFe-based hydroxide materials are the benchmark non-noble metal OER electrocatalysts with reduced cost and considerable activity [25–28]. To improve the intrinsic activity of NiFe hydroxides, a number of strategies have been proposed to regulate the surface electronic structure of such materials [29–32]. However, the electric conductivity properties, as an equally important factor that determines the intrinsic activity of an electrocatalyst, has received less attention [33,34]. More importantly, NiFe hydroxide materials are generally semiconducting or even insulating, and their poor conductivity has limited the electron transfer from the catalyst surface to the current collector, which has been a major deficiency that restricts the intrinsic activity of hydroxide materials. As a result, large overpotential is needed to overcome the energy barrier of interfacial proton-coupled electron transfer processes, leading to a low energy conversion efficiency [35,36]. Exploring NiFe hydroxide materials with excellent electrical properties to achieve highly intrinsic activity for OER is highly desirable yet a grand challenge.

In this study, we turned NiFe layered double hydroxide (NF LDH) from semi-conducting to semi-metallic (SM) by cationic doping and anionic vacancy manipulation. The SM LDH materials showed significantly improved electronic conductivity (2 orders of magnitude lower resistivity) compared with the NF LDH semiconductor. *In-situ* spectral and theoretical investigation revealed that the conductive SM LDH materials could be transformed to active oxyhydroxide intermediates with massive high-valance metal sites under low OER overpotentials. Consequently, the SM LDH catalyst showed a low overpotential of 236 mV at an OER current density of 10 mA cm^{-2}, far better than the commercial RuO_2 catalyst (316 mV). After assembling on a three-dimensional (3D) Ni foam, the overpotential of SM LDH array electrode was further decreased to 195 mV at 10 mA cm^{-2}. More importantly, the Pt/C||SM LDH array two-electrode device exhibited a low working potential of 1.49 V under an overall water splitting current density of 50 mA cm^{-2}, which was 240 mV lower than that of the Pt/C||RuO_2 counterpart. These results suggest that semi-metallic state hydroxides are a promising group of electrode material for efficient electrocatalysis.

[1] Faculty of Materials Science and Chemistry, China University of Geosciences, Wuhan 430074, China
[2] School of Energy and Environment, Department of Materials Science and Engineering, City University of Hong Kong, Kowloon Tong, Hong Kong 999077, China
[*] Corresponding author (email: caizhao@cug.edu.cn)

© Science China Press 2024

EXPERIMENTAL SECTION

Synthesis of NF LDH, SM LDH, and SM LDH array

The NF LDH materials were prepared by a co-precipitation process. Typically, 32.0 mmol $Ni(NO_3)_2{\cdot}6H_2O$ and 10.6 mmol $Fe(NO_3)_3{\cdot}9H_2O$ were dissolved in 40 mL deionized water to prepare solution A. 20.3 mmol NaOH and 20.3 mmol Na_2CO_3 were dissolved in 40 mL deionized water to form solution B. The solutions A and B were jointly injected to 40 mL deionized water at 60 °C with a rate of 40 mL h^{-1}. The mixed solution was then reacted at 10 °C for 6 h to produce a chartreuse precipitate, namely NF LDH.

The SM LDH materials were prepared by a co-precipitation method followed by an aqueous reduction process. The co-precipitation procedure was the same as that for NF LDH except employing 30.9 mmol $Ni(NO_3)_2{\cdot}6H_2O$, 9.6 mmol $Fe(NO_3)_3{\cdot}9H_2O$, 1.1 mmol $Co(NO_3)_2{\cdot}6H_2O$ and 1.1 mmol $Mn(NO_3)_2{\cdot}6H_2O$ to prepare solution A. A brown precipitate (NFCM LDH) was obtained by such co-precipitation method followed by an aqueous reduction process, namely, 20 mL of 5 mg mL^{-1} NFCM LDH solution was added to 40 mL of 3 mol L^{-1} $NaBH_4$ solution and stirred for 1 h. The SM LDH products were then obtained, washed with distilled water, and dried in a vacuum oven for further use.

The SM LDH array was prepared by a hydrothermal method followed by an aqueous reduction process. In a typical process, a piece of Ni foam (2 × 3 cm^2) was washed with 3 mol L^{-1} HCl, deionized water, and ethanol and then transferred to a 50-mL Teflon-lined autoclave containing 1.81 mmol $Ni(NO_3)_2{\cdot}6H_2O$, 0.56 mmol $Fe(NO_3)_3{\cdot}9H_2O$, 0.06 mmol $Co(NO_3)_2{\cdot}6H_2O$, 0.06 mmol $Mn(NO_3)_2{\cdot}6H_2O$, 25 mmol urea, and 40 mL distilled water. The autoclave was then sealed and heated at 120 °C for 10 h to prepare NFCM LDH array. Afterwards, the NFCM LDH array was immersed to a 40 mL of 3 mol L^{-1} $NaBH_4$ solution for 1 h, and the SM LDH array was consequently obtained. The mass loading of SM LDH on the array electrode was 1.4 mg cm^{-2}.

Structural characterizations

The morphologies and element distribution information of the materials were analyzed with field emission transmission electron microscopy (TEM, Tecnai G^2 F20) and field emission scanning electron microscopy (SEM, Hitachi, SU8010). The crystal structure was characterized by a Bruker AXSD8-FOCUS X-ray diffractometer (XRD, Cu-Kα radiation, λ = 1.5418 Å). X-ray photoelectron spectroscopy (XPS) analysis was carried out on an AXIS-ULTRA DLD XPS scanning microprobe. The electrical property was characterized by a Quantum Design physical property measurement (PPMS) system. Raman spectra were collected on a WITec Alpha 300R Raman microscopy system with 532-nm excitation. UV-vis spectroscopy was carried out on a PerkinElmer Lambda-950 spectrophotometer. Electron paramagnetic resonance (EPR) was carried out on a Bruker A300 magnetic resonance spectroscopy.

Electrochemical measurements

Electrochemical properties of the materials were investigated on a CHI 660E electrochemical workstation with a three-electrode system using graphite counter electrode, Hg/HgO reference electrode, and 1 mol L^{-1} KOH electrolyte. The working electrode was made by coating 20 μL catalyst ink on carbon fiber paper substrate (1 cm × 0.5 cm, electrical resistivity: 5 mΩ cm). The catalyst ink was prepared by mixing 2 mg carbon black, 5 mg catalyst powder, 10 μL Nafion, and 1 mL ethanol. The linear sweep voltammetry (LSV) was carried out with a low scan rate of 1 mV s^{-1} to minimize the capacitive current. All the LSV curves were *IR*-corrected, the internal resistance was obtained based on electrochemical impedance spectroscopy (EIS). The EIS was performed from 10 mHz to 100 kHz with an amplitude of 5 mV.

Computational details

DFT + *U* calculation was performed using a projector-augmented wave method and a plane-wave Basus set was implemented in the Vienna Simulation Package. The bulk and surface properties of LDH were studied within generalized gradient approximation and Perdew-Burke-Enzerhoff. Full optimization of the atom position in the bulk was performed *via* a conjugate gradient optimization procedure with the sum of the absolute forces less than 0.1 eV $Å^{-1}$. The bulk lattice constants were optimized using the 2 × 2 × 1 Monkhorst-Pack *k*-point sampling. The cut-off energy for plane-wave basis functions was set to 400 eV with the energy change convergence criterion of 1×10^{-4} eV. The vacuum thickness was set to be 15 Å, and the Hubbard-*U* was set as 3.8 eV for Co, 6.45 eV for Fe, 3.9 eV for Mn, and 5.3 eV for Ni.

RESULTS AND DISCUSSION

To screen hydroxide materials with narrowed bandgap and improved electrical properties, density functional theory with Hubbard *U* correction (DFT + *U*) computation was employed. As shown in Fig. 1a, b, the Femi level (E_f) of NiFe LDH was located near the valance band (VB) edge with a band gap of 1.75 eV, which is a typical value of semiconductor (1–3.4 eV) [37]. Cationic doping would increase the VB of NiFe LDH, but the VB edge was still far from E_f. Typically, after the introduction of Co and Mn cations, the NiFeCoMn LDH also showed a semiconductor nature with a band gap of 1.21 eV (Fig. 1a and Fig. S1). Introducing oxygen vacancies would significantly lower the conduction band (CB) edge of NiFe LDH, thus reducing the band gap of LDH. However, the atomic structure of LDH turned to be unstable with a large number of anionic vacancy defect, which was crashed during DFT modeling. The minimum band gap of stable NiFe LDH with oxygen vacancies (O_v-NiFe LDH) was calculated to be 0.65 eV (Fig. 1a and Fig. S2), which is much smaller than that of the pristine one, but still greater than 0 eV. Interestingly, when combining the cationic doping and anionic vacancy regulation, the CB edge of NiFeCoMn LDH with oxygen vacancies (O_v-NiFeCoMn LDH) would meet the VB edge with a band gap of 0 eV, suggesting the semi-metallic nature of O_v-NiFeCoMn LDH with good structural stability.

In order to experimentally confirm whether O_v-NiFeCoMn LDH is semi-metallic, a co-precipitation process followed by a liquid-phase reduction reaction was adopted to fabricate the as-proposed O_v-NiFeCoMn LDH materials. UV-vis spectroscopy was first utilized to determine the band gap energy (E_g) of the as-prepared NiFe LDH (i.e. NF LDH) and O_v-NiFeCoMn LDH (i.e., SM LDH). As shown in Fig. 1d, the evaluated E_g value for NF LDH was 2.18 eV while it was 0 eV for SM LDH, in good accord with the theoretical finding. Furthermore, the temperature-dependent electrical resistivities of NF LDH and SM LDH materials were studied and shown in Fig. 1e. The electrical resistivity of the as-prepared NF LDH was monotonically

© Science China Press 2024

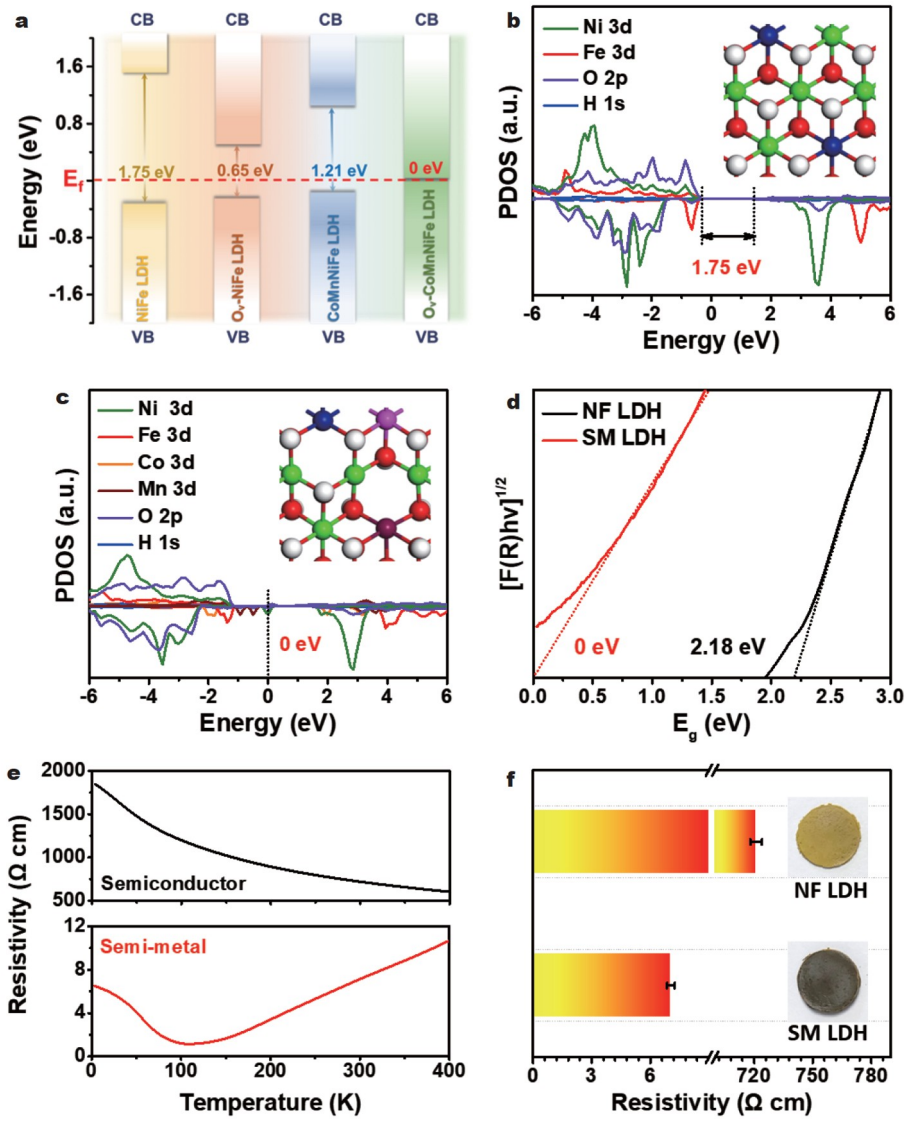

Figure 1 Design of SM LDH. (a) Schematic illustration of the band gaps for NiFe LDH, O_v-NiFe LDH, NiFeCoMn LDH, and O_v-NiFeCoMn LDH. Calculated partial density of states for (b) NiFe LDH and (c) O_v-NiFeCoMn LDH. The insets show the atomic structure of NiFe LDH/O_v-NiFeCoMn LDH for calculation (Green: Ni; Navy: Fe; Pink: Co; Brown: Mn; Red: O; White: H). (d) Optical band gap energy determination of NF LDH and SM LDH. (e) Temperature-dependent electrical resistivity of NF LDH semiconductor and SM LDH semi-metallic materials. (f) The electrical resistivities of NF LDH and SM LDH at room temperature. The error bars were obtained by repeating the measurements for five times. The insets show the digital images of the NF LDH and SM LDH plates for electrical measurements.

decreased along with the temperature increasing from 2 to 400 K, presenting a typical semiconductor characteristic. Interestingly, the electrical resistivity of the as-prepared SM LDH was decreased from 2 to 110 K, and then increased from 110 to 400 K. Such resistivity trend against temperature suggested a typical semi-metal property [38,39], indicating the semi-metallic nature of O_v-NiFeCoMn LDH. In addition, the color of the SM LDH materials turned to be much darker compared with that of conventional NF LDH, suggesting the altered visible absorptance even by naked eye, which was a piece of direct evidence for the regulated electronic properties of SM LDH (inset in Fig. 1f). Moreover, it was uncovered that the electrical resistivity of SM LDH was only 7.1 Ω cm at room temperature, two orders of magnitude lower than that of NF LDH 721.4 Ω cm, suggesting the significantly improved electronic conductivity of the as-designed SM LDH material.

The representative TEM images reveal a typical sheet morphology of SM LDH with an average size of 135 nm and an average thickness of 2.66 nm (Fig. 2b), which is similar to that of NF LDH (143 nm in size, 2.46 nm in thickness, Fig. 2a). The energy dispersive spectroscopy (EDS) elemental mapping results of SM LDH confirm the successful introduction of Co and Mn dopants to NF LDH (Fig. 2c and Fig. S3). The EDS spectra suggest the atomic ratio of Ni/Fe/Co/Mn is 71.2/23.1/2.8/2.9 in SM LDH (Fig. S4, Table S1), which is the same as that of O_v-NiFeCoMn LDH for theoretical modeling in Fig. 1c. The O 1s XPS of SM LDH shows an increase in unsaturated O species (69.3%) compared with NF LDH (20.4%) and NFCM LDH (25.7%), suggesting the introduction of massive oxygen vacancies by $NaBH_4$ reduction (Fig. 2d and Fig. S5). Moreover, a broader and stronger signal of SM LDH in EPR (Fig. S6) demonstrates a defect-richer structure compared with that of NF

© Science China Press 2024

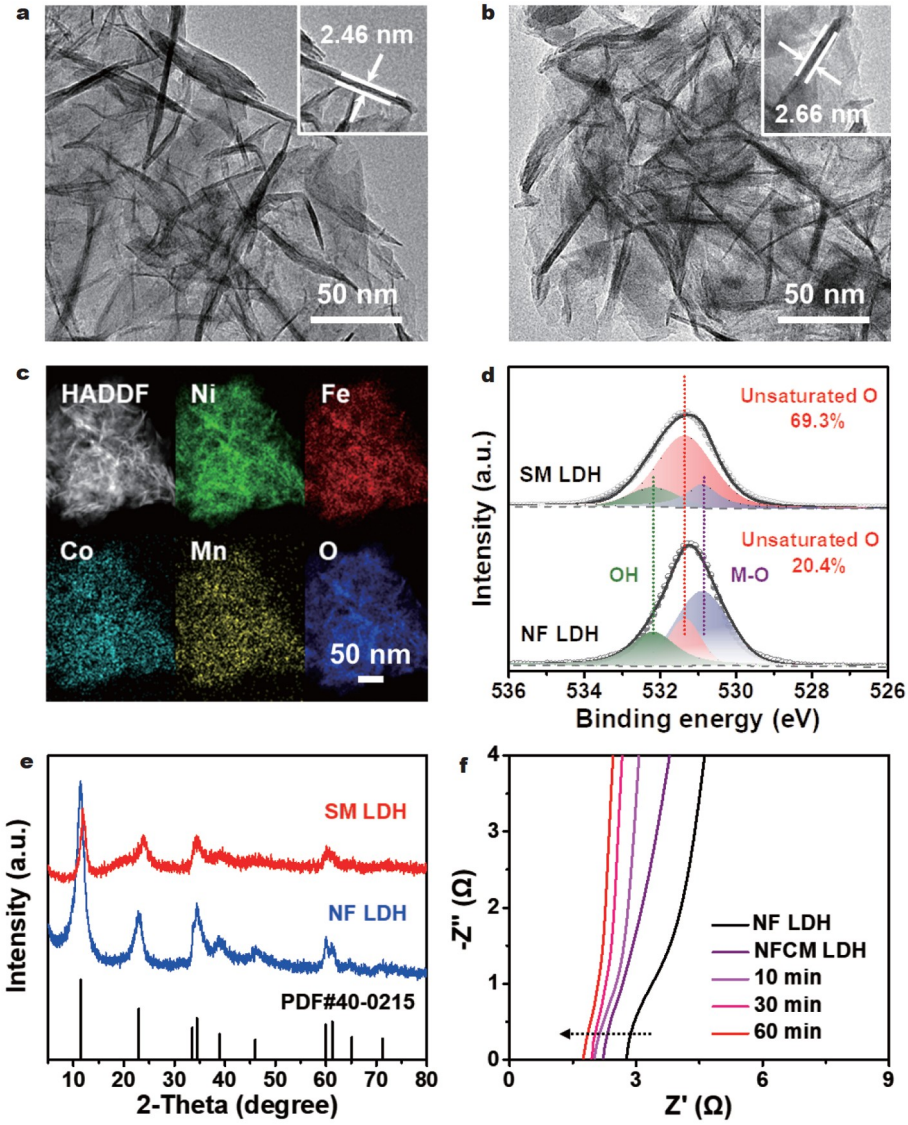

Figure 2 Structural and electronic properties of SM LDH. TEM images of (a) NF LDH and (b) SM LDH nanosheets. The insets show the thicknesses of NF LDH and SM LDH, respectively. (c) High angle annular dark field and EDS elemental mapping images of SM LDH nanosheets. (d) O 1s XPS spectra of NF LDH and SM LDH, suggesting the introduction of oxygen vacancies in SM LDH. (e) XRD analyses of NF LDH and SM LDH materials, indicating the lattice shrinkage of SM LDH. (f) *In-situ* EIS results of SM LDH during $NaBH_4$ reduction, indicating the reduced solution resistance.

LDH. The signal of SM LDH at $g = 2.0005$ indicates the electrons trapped on oxygen vacancies, in agreement with the XPS results in Fig. 2d. The XRD analysis in Fig. 2e suggests that SM LDH maintains the crystal structure of NF LDH after the introduction of cationic Co/Mn dopants and anionic oxygen vacancies. However, the diffraction peaks of SM LDH shifts to higher degrees, suggesting a lattice shrinkage. The high-resolution TEM images also confirm the reduced lattice spacing of SM LDH comparing with that of NF LDH (Figs S7, S8). Furthermore, EIS was employed to analyze the electrochemical properties of SM LDH during synthesis. Since the solution resistance is the resistance between the working and the reference electrodes, and the reference electrode, the electrolyte, carbon fiber paper substrate, conductive additive, and binder materials were identical during EIS measurements, such solution resistance difference was only attributed to the electrical resistance of the LDH materials. As shown in Fig. 2f, NiFeCoMn LDH (NFCM LDH) shows a smaller solution resistance (2.3 Ω) than NF LDH (2.8 Ω), suggesting the improved electronic conductivity. Moreover, the solution resistances of NFCM LDH were further decreased after aqueous $NaBH_4$ reduction for different times (2.1 Ω for 20 min, and 1.9 Ω for 40 min). Notably, after 60 min of reduction, the as-prepared SM LDH was turned to a black color (Fig. S9) and exhibited the smallest solution resistance of 1.7 Ω, suggesting the excellent electron-conductivity, in accord with the computational analysis in Fig. 1a–c.

The improved electronic conductivity of SM LDH could enhance the electrocatalytic intrinsic activity. As shown in Fig. 3a and Fig. S10, the SM LDH displays a low overpotential of 236 mV at 10 mA cm^{-2}, which is 14, 27, 64 and 80 mV lower than that of O_v-NF LDH, NFCM LDH, NF LDH, and commercial RuO_2 catalysts, respectively. The electrochemical surface area of the catalysts was evaluated by measuring the double-layer capacitance, the OER activity of SM LDH normalized by the

 © Science China Press 2024

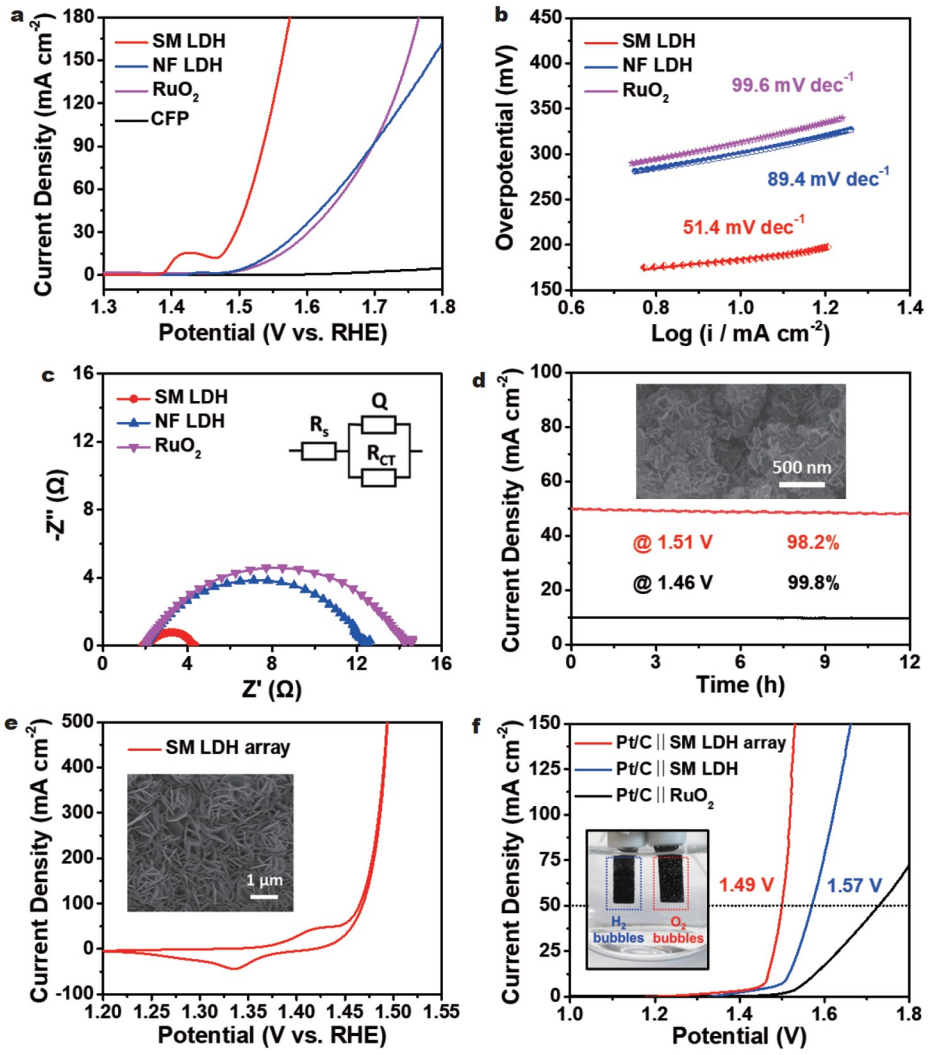

Figure 3 Electrocatalytic OER performance of SM LDH. (a) OER polarization curves, (b) Tafel plots, and (c) EIS results of SM LDH, NF LDH, and commercial RuO_2 catalysts. (d) Chronopotentiometric curves for SM LDH material at OER current densities of 10 and 50 mA cm^{-2}. The inset shows the SEM image of SM LDH after 12-h stability test at 50 mA cm^{-2}. (e) The OER polarization curve of SM LDH array electrode. The inset shows the SEM image of SM LDH array. (f) Overall water splitting polarization curves for SM LDH array, SM LDH, and commercial RuO_2 OER catalysts pairing with a Pt/C HER catalyst. The inset shows the Pt/C||SM LDH array two-electrode set-up powered by a 1.5-V dry battery.

electrochemical surface area was also higher than that of NF LDH (Fig. S11). The improved intrinsic activity of SM LDH was further confirmed by the Tafel plots in Fig. 3b, where SM LDH exhibited the smallest Tafel slope of 51.4 mV dec^{-1}. EIS was also applied under an OER potential of 1.5 V, the equivalent circuit used for EIS fitting was shown in the inset of Fig. 3c, and SM LDH shows a charge transfer resistance of 2.3 Ω, which is much smaller than NF LDH (10.2 Ω) and RuO_2 (12.3 Ω). Moreover, SM LDH also exhibited the smaller solution resistance of 1.7 Ω, when compared with NF LDH (2.1 Ω), and RuO_2 catalysts (2.2 Ω) (Fig. S12), indicating the highest electronic conductivity of SM LDH during OER working conditions, which should be beneficial for the improvement in the intrinsic activity for OER. The SM LDH also shows a long-term catalytic stability at the current densities of 10 and 50 mA cm^{-2} (Fig. 3d), while the SEM image of SM LDH after electrochemical stability test at 50 mA cm^{-2} for 12 h in the inset of Fig. 3d further confirms the stability of the material. XPS characterization indicates that the content of unsaturated O species for the SM LDH after OER stability measurements (68.8%, Fig. S13) is nearly the same as that before OER (69.3%, Fig. 2d), suggesting the high stability of oxygen vacancy defects in SM LDH materials. Moreover, SM LDH was assembled on a 3D Ni foam (denoted as SM LDH array) to further optimize the OER performance. As shown in Fig. 3e and Fig. S14, the SM LDH array exhibits a low overpotential of 195 mV at 10 mA cm^{-2} with a low Tafel slope of 40.9 mV dec^{-1}, which is among the best-performed LDH-based OER electrocatalyst to date (Figs S15, S16). The SM LDH array electrode also shows outstanding OER stability under high current density of 400 mA cm^{-2} (Fig. S17). Motivated by the excellent OER performance, we tested the overall water splitting performance of SM LDH after pairing with a commercial Pt/C cathode (Fig. 3f). The Pt/C||SM LDH array shows a low water splitting potential of 1.49 V at 50 mA cm^{-2}, which is 80 and 240 mV lower than the Pt/C||SM LDH and Pt/C||RuO_2 counterparts, respectively. The Pt/C||SM LDH array two-electrode device could be powered by a 1.5 V dry battery, as shown in the inset of Fig. 3f, where significant hydrogen and oxygen bubbles

© Science China Press 2024

could be observed, suggesting the excellent electrocatalytic performance and practicality of the as-achieved SM LDH materials.

To get deeper insights into the improved intrinsic activity of SM LDH, *in-situ* Raman (Fig. S18) and DFT studies were carried out. As shown in Fig. 4a, NF LDH showed two distinct peaks at 454 and 531 cm^{-1} at open circuit voltage (OCV), which came from the $Ni(OH)_2$ phase in NF LDH [40,41]. As an external overpotential applied (from 50 to 250 mV), the peak intensity of $Ni(OH)_2$ was gradually decreased. However, under a large overpotential of 350 mV, no distinct signal of oxyhydroxide such as NiOOH could be detected, suggesting no formation of conductive oxyhydroxide intermediates, which was attributed to the low electrical conductivity, and could be responsible for the low intrinsic activity for OER. SM LDH also showed two $Ni(OH)_2$ peaks at 454 and 531 cm^{-1} at OCV, which decreased with an applied external overpotentials (50 mV). Notably, vibrational peaks at 578 and 623 cm^{-1} corresponding to CoOOH and MnOOH could be observed for SM LDH at 150 mV [42,43], which even turned stronger at 250–350 mV, suggesting the formation of oxyhydroxide intermediates. Noted that the CoOOH and MnOOH peaks showed some deviation, and were so broad to blended into each other. This could be attributed to the highly disordered oxyhydroxide structure at 350 mV, since the disordered phase generally exhibits broadened and positively shifted Raman vibration peaks [44,45]. In addition, since the transformation from hydroxide to oxyhydroxide is a proton-coupled electron transfer process (Fig. S19), the high conductivity of SM LDH would accelerate the reaction kinetics of such transformation process, therefore promoting the stabilization of metal sites in oxyhydroxide intermediates, which could

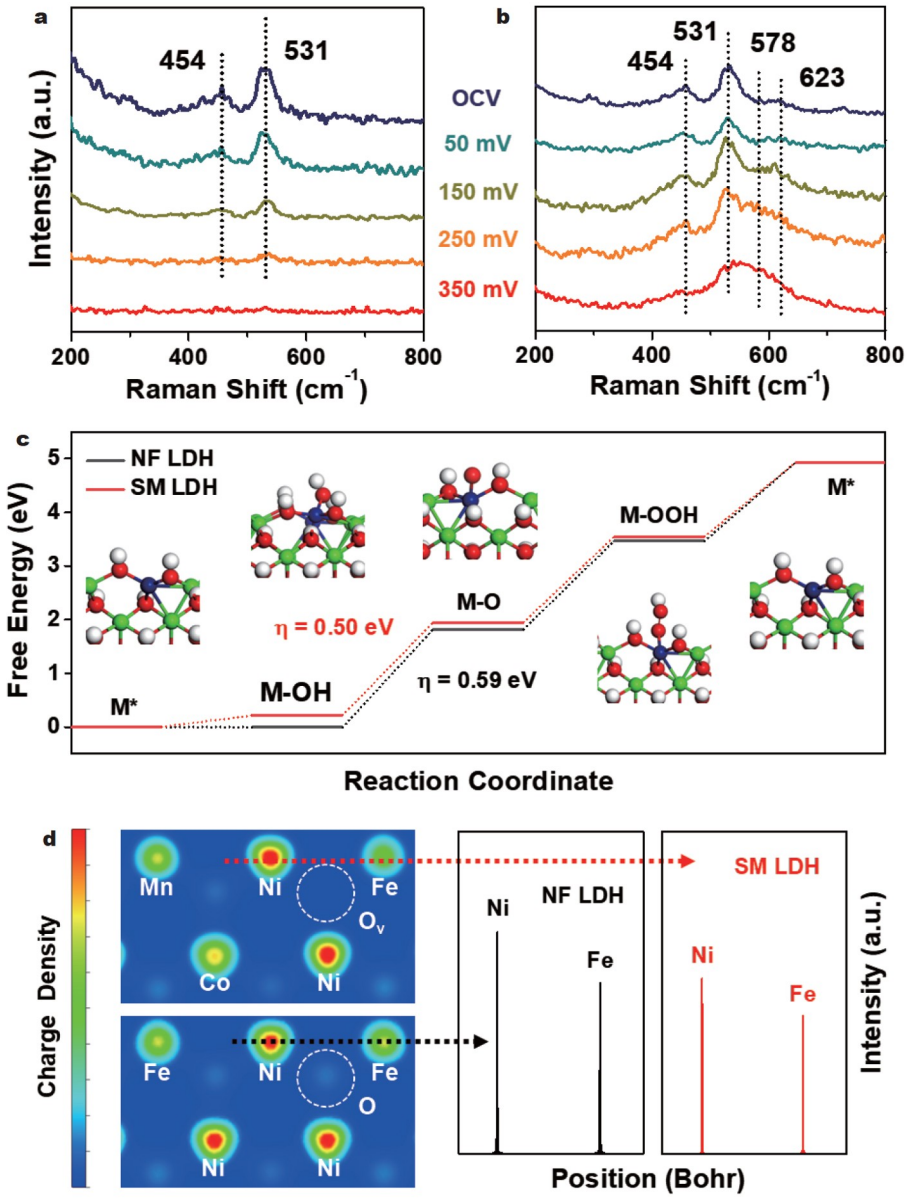

Figure 4 Mechanism of the improved intrinsic activity. *In-situ* Raman analysis of (a) NF LDH and (b) SM LDH materials within an OER overpotential range of 0–350 mV. (c) Free energy plots of NF LDH and SM LDH catalysts for OER. The insets show the atomic structures of the OER intermediates for calculation. (d) Local charge density maps and Ni/Fe site charge density analysis of NF LDH and SM LDH catalysts for the deprotonation step, suggesting the higher valance states of Ni and Fe sites for SM LDH during OER.

© Science China Press 2024

be responsible for the enhanced intrinsic OER activity.

The DFT calculation was also conducted to study the thermodynamic/electronic properties of SM LDH during OER, an unsaturated Fe atom at the edge of LDH structure was selected as the catalytic active site and NF LDH was also calculated for comparison (Fig. 4c). As the standard 4e⁻ OER mechanism proposed by Nørskov [46] was applied, the rate determining step of SM LDH was found to be the deprotonation of the adsorbed OH with an overpotential of 0.50 eV, which was much lower than that of NF LDH (0.59 eV), suggesting the improved intrinsic catalytic activity for SM LDH. Moreover, the charge density of the metal sites for NF LDH and SM LDH during the deprotonation step was analyzed. As shown in the Fig. 4d, the charge density map indicated the lower electron density of both Ni and Fe sites in the M-O intermediates for SM LDH compared with that for NF LDH, suggesting a higher valance state of these active metal sites during OER [47], which was in consistent with the *in-situ* Raman results in Fig. 4a, b. These findings suggest that the improved electronic conductivity of SM LDH facilitates the electrochemical transformation of hydroxide to oxyhydroxide intermediates and the stabilization of high valance sites during OER, thus improving the intrinsic electrocatalytic activity for OER [48].

CONCLUSIONS

In summary, a semi-metallic hydroxide was developed as efficient OER electrocatalyst materials. The two orders of magnitude improved electronic conductivity favors the hydroxide to oxyhydroxide transformation under OER working conditions, thus stabilizing high-valance active sites at low overpotentials for intrinsically high electrocatalytic activity. The as-designed SM LDH array electrode exhibited a low OER overpotential of 195 mV at 10 mA cm^{-2} and a small Tafel slope of 40.9 mV dec^{-1}. Moreover, the SM LDH array electrode achieved an ultralow potential of 1.49 V at a water splitting current density of 50 mA cm^{-2} after pairing with a commercial Pt/C cathode catalyst, which was 240 mV lower than that of the Pt/C||RuO_2 counterpart. This study not only sheds light on the exploration of advanced hydroxide electrocatalysts with excellent electronic properties, but also inspires the design of conducting electrode materials for renewable energy conversion technologies.

Received 6 December 2023; accepted 29 January 2024; published online 12 April 2024

1 Mefford JT, Akbashev AR, Kang M, *et al.* Correlative *operando* microscopy of oxygen evolution electrocatalysts. Nature, 2021, 593: 67–73
2 Kang J, Qiu X, Hu Q, *et al.* Valence oscillation and dynamic active sites in monolayer NiCo hydroxides for water oxidation. Nat Catal, 2021, 4: 1050–1058
3 Shi H, Wang T, Liu J, *et al.* A sodium-ion-conducted asymmetric electrolyzer to lower the operation voltage for direct seawater electrolysis. Nat Commun, 2023, 14: 3934
4 Zhang Y, Cai Z, Zhao Y, *et al.* Superaerophilic copper nanowires for efficient and switchable CO_2 electroreduction. Nanoscale Horiz, 2019, 4: 490–494
5 Xiong P, Tan J, Lee H, *et al.* Two-dimensional carbon-based heterostructures as bifunctional electrocatalysts for water splitting and metal–air batteries. Nano Mater Sci, 2022, doi: 10.1016/j.nanoms.2022.10.001
6 Chen M, Kitiphatpiboon N, Feng C, *et al.* Recent progress in transition-metal-oxide-based electrocatalysts for the oxygen evolution reaction in natural seawater splitting: A critical review. eScience, 2023, 3: 100111
7 Zhou Y, Li C, Zhang Y, *et al.* Controllable thermochemical generation of active defects in the horizontal/vertical MoS_2 for enhanced hydrogen evolution. Adv Funct Mater, 2023, 33: 2304302
8 Li G, Duan X, Liu X, *et al.* Locking active Li metal through localized redistribution of fluoride enabling stable Li-metal batteries. Adv Mater, 2023, 35: 2207310
9 Zhang N, Hu Y, An L, *et al.* Surface activation and Ni-S stabilization in NiO/NiS_2 for efficient oxygen evolution reaction. Angew Chem Int Ed, 2022, 61: e202207217
10 Chen YF, Li JH, Liu TT, *et al.* Constructing robust NiFe LDHs–NiFe alloy gradient hybrid bifunctional catalyst for overall water splitting: one-step electrodeposition and surface reconstruction. Rare Met, 2023, 42: 2272–2283
11 Xie R, Luo W, Zou L, *et al.* Low-temperature synthesis of colloidal few-layer WTe_2 nanostructures for electrochemical hydrogen evolution. Discover Nano, 2023, 18: 44
12 Jia B, Zhang B, Cai Z, *et al.* Construction of amorphous/crystalline heterointerfaces for enhanced electrochemical processes. eScience, 2023, 3: 100112
13 Cai Z, Bi Y, Hu E, *et al.* Single-crystalline ultrathin Co_3O_4 nanosheets with massive vacancy defects for enhanced electrocatalysis. Adv Energy Mater, 2017, 8: 1701694
14 Lee YJ, Park SK. Synergistically coupling of Ni–Fe LDH arrays with hollow Co–Mo sulfide nanotriangles for highly efficient overall water splitting. Rare Met, 2024, 43: 522–532
15 Zhu H, Sun S, Hao J, *et al.* A high-entropy atomic environment converts inactive to active sites for electrocatalysis. Energy Environ Sci, 2023, 16: 619–628
16 Xiao Z, Zhou W, Yang B, *et al.* Tuned d-band states over lanthanum doped nickel oxide for efficient oxygen evolution reaction. Nano Mater Sci, 2023, 5: 228–236
17 Xu X, Wang S, Guo S, *et al.* Cobalt phosphosulfide nanoparticles encapsulated into heteroatom-doped carbon as bifunctional electrocatalyst for Zn−air battery. Adv Powder Mater, 2022, 1: 100027
18 Lin R, Kang L, Zhao T, *et al.* Identification and manipulation of dynamic active site deficiency-induced competing reactions in electrocatalytic oxidation processes. Energy Environ Sci, 2022, 15: 2386–2396
19 Duan X, Getaye Sendeku M, Zhang D, *et al.* Tungsten-doped NiFe-layered double hydroxides as efficient oxygen evolution catalysts. Acta Physico Chim Sin, 2023, 0: 2303055
20 Han X, Li N, Baik JS, *et al.* Sulfur mismatch substitution in layered double hydroxides as efficient oxygen electrocatalysts for flexible zinc–air batteries. Adv Funct Mater, 2023, 33: 2212233
21 Deng R, Guo M, Wang C, *et al.* Recent advances in cobalt phosphide-based materials for electrocatalytic water splitting: From catalytic mechanism and synthesis method to optimization design. Nano Mater Sci, 2022, doi: 10.1016/j.nanoms.2022.04.003
22 Chen L, Wang H, Tan L, *et al.* PEO-PPO-PEO induced holey NiFe-LDH nanosheets on Ni foam for efficient overall water-splitting and urea electrolysis. J Colloid Interface Sci, 2022, 618: 141–148
23 Wang L, Zhang L, Ma W, *et al.* *In situ* anchoring massive isolated Pt atoms at cationic vacancies of α-$Ni_xFe_{1-x}(OH)_2$ to regulate the electronic structure for overall water splitting. Adv Funct Mater, 2022, 32: 2203342
24 Hu R, Wei L, Xian J, *et al.* Microwave shock process for rapid synthesis of 2D porous $La_{0.2}Sr_{0.8}CoO_3$ perovskite as an efficient oxygen evolution reaction catalyst. Acta Physico Chim Sin, 2023, 0: 2212025
25 Duan X, Li T, Jiang X, *et al.* Catalytic applications of single-atom metal-anchored hydroxides: Recent advances and perspective. Mater Rep-Energy, 2022, 2: 100146
26 Xie Q, Cai Z, Li P, *et al.* Layered double hydroxides with atomic-scale defects for superior electrocatalysis. Nano Res, 2018, 11: 4524–4534
27 Wang H, Chen L, Tan L, *et al.* Electrodeposition of NiFe-layered double hydroxide layer on sulfur-modified nickel molybdate nanorods for highly efficient seawater splitting. J Colloid Interface Sci, 2022, 613: 349–358
28 Wang Z, Wang C, Ye L, *et al.* MnO_x film-coated NiFe-LDH nanosheets on Ni foam as selective oxygen evolution electrocatalysts for alkaline seawater oxidation. Inorg Chem, 2022, 61: 15256–15265
29 Bi Y, Cai Z, Zhou D, *et al.* Understanding the incorporating effect of Co^{2+}/Co^{3+} in NiFe-layered double hydroxide for electrocatalytic oxygen

© Science China Press 2024

evolution reaction. J Catal, 2018, 358: 100–107
30 Luo M, Cai Z, Wang C, *et al.* Phosphorus oxoanion-intercalated layered double hydroxides for high-performance oxygen evolution. Nano Res, 2017, 10: 1732–1739
31 Cai Z, Zhou D, Wang M, *et al.* Introducing Fe^{2+} into nickel–iron layered double hydroxide: local structure modulated water oxidation activity. Angew Chem Int Ed, 2018, 57: 9392–9396
32 Tan L, Yu J, Wang C, *et al.* Partial sulfidation strategy to NiFe-LDH@$FeNi_2S_4$ heterostructure enable high-performance water/seawater oxidation. Adv Funct Mater, 2022, 32: 2200951
33 Huang C, Zhou Q, Duan D, *et al.* The rapid self-reconstruction of Fe-modified Ni hydroxysulfide for efficient and stable large-current-density water/seawater oxidation. Energy Environ Sci, 2022, 15: 4647–4658
34 Xiong X, Cai Z, Zhou D, *et al.* A highly-efficient oxygen evolution electrode based on defective nickel-iron layered double hydroxide. Sci China Mater, 2018, 61: 939–947
35 Bao Y, Lian C, Huang K, *et al.* Generating high-valent iron-oxo $\equiv Fe^{IV}=O$ complexes in neutral microenvironments through peroxymonosulfate activation by Zn−Fe layered double hydroxides. Angew Chem Int Ed, 2022, 61: e202209542
36 Yuan Z, Bak SM, Li P, *et al.* Activating layered double hydroxide with multivacancies by memory effect for energy-efficient hydrogen production at neutral pH. ACS Energy Lett, 2019, 4: 1412–1418
37 Xin K, Yang W, Xia J, *et al.* Research progress of ultra-wide bandgap two-dimensional semiconductor materials and devices. Sci Sin-Phys Mech Astron, 2022, 52: 297302
38 Kumar N, Shekhar C, Wu SC, *et al.* Observation of pseudo-two-dimensional electron transport in the rock salt-type topological semimetal LaBi. Phys Rev B, 2016, 93: 241106
39 Zhao Y, Zhang X, Jia X, *et al.* Sub-3 nm ultrafine monolayer layered double hydroxide nanosheets for electrochemical water oxidation. Adv Energy Mater, 2018, 8: 1703585
40 Faid AY, Barnett AO, Seland F, *et al.* Ni/NiO nanosheets for alkaline hydrogen evolution reaction: In situ electrochemical-Raman study. Electrochim Acta, 2020, 361: 137040
41 Qiu Z, Tai CW, Niklasson GA, *et al.* Direct observation of active catalyst surface phases and the effect of dynamic self-optimization in NiFe-layered double hydroxides for alkaline water splitting. Energy Environ Sci, 2019, 12: 572–581
42 Jing C, Yuan T, Li L, *et al.* Electrocatalyst with dynamic formation of the dual-active site from the dual pathway observed by *in situ* Raman spectroscopy. ACS Catal, 2022, 12: 10276–10284
43 Lan L, Li Q, Gu G, *et al.* Hydrothermal synthesis of γ-MnOOH nanorods and their conversion to MnO_2, Mn_2O_3, and Mn_3O_4 nanorods. J Alloys Compd, 2015, 644: 430–437
44 Enkhtuvshin E, Yeo S, Choi H, *et al.* Surface reconstruction of Ni–Fe layered double hydroxide inducing chloride ion blocking materials for outstanding overall seawater splitting. Adv Funct Mater, 2023, 33: 2214069
45 Trześniewski BJ, Diaz-Morales O, Vermaas DA, *et al.* In situ observation of active oxygen species in Fe-containing Ni-based oxygen evolution catalysts: the effect of pH on electrochemical activity. J Am Chem Soc, 2015, 137: 15112–15121
46 Friebel D, Louie MW, Bajdich M, *et al.* Identification of highly active Fe sites in (Ni,Fe)OOH for electrocatalytic water splitting. J Am Chem Soc, 2015, 137: 1305–1313
47 Lu T, Chen F. Multiwfn: A multifunctional wavefunction analyzer. J Comput Chem, 2012, 33: 580–592
48 Zhou L, Zhang C, Zhang Y, *et al.* Host modification of layered double hydroxide electrocatalyst to boost the thermodynamic and kinetic activity of oxygen evolution reaction. Adv Funct Mater, 2021, 31: 2009743

Acknowledgements This work was financially supported by the National Natural Science Foundation of China (22205068 and 22109144), the "CUG Scholar" Scientific Research Funds at China University of Geosciences (Wuhan) (2022118), and the Fundamental Research Funds for the Central Universities, China University of Geosciences (Wuhan) (162301202673). We appreciate eceshi (www.eceshi.com) and Shiyanjia Lab (www.shiyanjia.com) for the PPMS analyses. Thanks to the *in-situ* Raman electrochemical cell from Hefei *In-situ* Technology. Co., Ltd.

Author contributions Wang J, Zhou C and Cai Z conceived the project. Wang J, Gao Q, Han B, Sun R and Zhao C performed the experiments. Wang J, Jamesh MI, Hsu HY and Cai Z wrote the manuscript. Cai Z and Zhou C supervised the project. All authors discussed the results and commented on the manuscript.

Conflict of interest The authors declare that they have no conflict of interest.

Supplementary information Experimental details and supporting data are available in the online version of the paper.

Jing Wang received her Bachelor and Master's degrees from China University of Geoscience (Wuhan) in 2019 and 2022, respectively. She is pursuing her doctoral degree under the supervision of Prof. Zhao Cai at China University of Geoscience (Wuhan). Her research interests mainly focus on transition metal-based nanomaterials for electrocatalysis.

Zhao Cai gained his BS degree and PhD in Chemistry from Beijing University of Chemical Technology in 2012 and 2018, respectively. After working as a visiting scholar at Yale University and postdoctoral researcher at Wuhan National Laboratory for Optoelectronics, he joined China University of Geosciences (Wuhan) as a professor of chemistry in 2022. His research focuses on developing novel transition metal nanostructures for key energy conversion and storage processes, such as electrocatalysis and aqueous batteries.

半金属氢氧化物材料用于电化学水氧化

王静[1], Mohammed-Ibrahim Jamesh[2], 高强[1], 韩波[1], 孙睿敏[1], Hsien-Yi Hsu[2], 周成冈[1], 蔡钊[1*]

摘要 寻找具有高本征活性的水氧化催化剂材料对许多清洁能源技术的发展至关重要. 氢氧化物半导体对析氧反应具有一定的电催化活性. 然而, 该材料导电性较差, 限制着其电催化本征活性的提升. 本文提出一种兼具高导电性和高催化活性的半金属氢氧化物析氧电催化材料. 通过阳离子掺杂和阴离子空位协同作用, 镍铁水滑石半导体可转化为半金属材料, 其电阻率降低了两个数量级. 相应半金属氢氧化物阵列电极的电催化活性显著提升, 在10 mA cm^{-2}电流密度下其析氧过电势仅为195 mV, Tafel斜率仅为40.9 mV dec^{-1}, 显著优于商用RuO_2催化剂(316 mV, 99.6 mV dec^{-1}). 原位拉曼光谱和理论计算结果表明, 半金属氢氧化物可在较低过电位下转化为羟基氧化物中间体, 有助于高价态金属活性位点的形成与稳定, 从而提升材料的析氧本征活性. 本研究表明, 兼具优异导电性和催化活性的半金属氢氧化物可作为先进的电极材料.

 © Science China Press 2024